AIAA JOURNAL
Vol. 43, No. 2, February 2005

Sound Generated by a Pair of Axisymmetric Coaxial Vortex Rings

Y. S. K. Liow,* M. C. Thompson,† and K. Hourigan‡
Monash University, Melbourne, Victoria 3800, Australia

The time-dependent acoustic field generated by the mutual interaction of a pair of coaxial viscous vortex rings advecting along a common axis of symmetry is simulated using a two-step numerical procedure. In the first step, the flowfield is predicted by solving the incompressible Navier–Stokes equations. In the second step, Powell's vortex sound theory is used to predict the far-field acoustic field associated with the flow unsteadiness. This study considers the effect of the initial toroidal ring radii on the sound radiation. The acoustic predictions are compared with those obtained using the method of matched asymptotic expansions. Our results indicate that the acoustic signature for the Mach-number range simulated shows an axisymmetric lateral quadrupole pattern. In addition, the time variation of the far-field acoustic signal displays significant effects caused by vortex dynamics associated with the finite-sized cores and viscous diffusion. These effects are more pronounced for rings with a smaller initial toroidal radius. The influence of Mach number on the far-field directivity (e.g., location of polar extinction angles) and the multipole content of the acoustic signal is examined through a multipole decomposition of the predicted acoustic fields.

I. Introduction

In this study, Powell's[1] theory of vortex sound is used to predict the far-field sound generated by the pairing of two axisymmetric viscous vortex rings. Powell[1] has hypothesized that at low Mach numbers sound is a byproduct of the flow. Therefore, the sound energy does not feed back toward the flowfield. Instead, the sound waves are generated by the flow unsteadiness in the near field and are subsequently propagated to the far field in an ambient medium. The source of the acoustic fluctuations is attributed to the motion as well as the change in strength of the vorticity field, that is, rotational part in the near-field region. The validity of Powell's[1] vortex sound theory has been confirmed by various investigators through comparison with other prediction tools such as direct numerical simulations[2] and experimental results.[3]

Implementation-wise, the decoupling of the flow and acoustic fields involves a two-step numerical approach toward obtaining the acoustic solution. First, the incompressible flow is predicted by solving the incompressible Navier–Stokes equations. Next, the acoustic quantities are obtained through solving the inhomogeneous wave equation, with the acoustic source terms evaluated from the hydrodynamic velocity field. The numerical method used in this study has been successfully adopted in an earlier investigation.[4] Therefore, the motivation behind this study is that it serves as a second benchmarking study in the development of the two-step aeroacoustic prediction method currently being developed by the Fluids Laboratory for Aeronautical and Industrial Research group.

From a historical perspective, thin vortex cores have been widely used in theoretical aeroacoustics (for instance, Refs. 5 and 6) because of two important factors. First, by taking the approximation of an infinitesimally thin vortex core (i.e., a potential flow vortex) and an inviscid fluid, the hydrodynamic and acoustic solution can often be obtained analytically. Second, for low-Mach-number flows, the characteristic length scale of the flow is much smaller than the acoustic wavelength allowing a mathematical separation into a near-field hydrodynamic region and far-field acoustic region.

Under such idealized conditions, the leapfrogging cycle of a pair of like-signed vortex rings would repeat itself indefinitely without any core deformation.[5–8] Using the method of matched asymptotic expansions (MAE), Kambe and Minota[6] predicted that the sound field would assume an axisymmetric lateral quadrupole pattern. By comparing the trajectories of the vortex rings with the time histories of the acoustic pressure fluctuations, the latter was found to peak at the instant when the radial distance between the vortex rings was a maximum. In addition, owing to the symmetry of the motion, the frequency of the acoustic oscillations is twice that of the leapfrogging frequency.

The assumption of an infinitesimally thin ring is a mathematical abstraction, as in reality vortex rings are finite. The acoustic radiation from rings having a finite core has been considered by, among others, Shariff et al.[9] and Tang and Ko.[10] The motion of these inviscid, finite-sized vortex rings was predicted using the method of contour dynamics. In contrast to Kambe and Minota,[6] Shariff et al.[9] and Tang and Ko[10] predicted the presence of an additional high-frequency component superimposed on the one associated with the leapfrogging motion. This was attributed by both authors to the distortion of the vortex core caused by the strain field imposed on each core by the other during the leapfrogging motion.

Verzicco et al.[11] considered the case of a pair of viscous vortex rings by solving the incompressible flow equations, and subsequently, used the solution field to calculate the acoustic sources based on Kambe's[12] analysis. They considered the effects of Reynolds number, different vorticity profiles, and core thicknesses. Results showed that sound generation is most intense when the vorticity gradients of the core are sharp. Furthermore, they have argued that the secondary acoustic source (associated with the nutation of the vortex core) is not a major contribution to the sound radiation from the pairing of a viscous vortex ring.

Another interesting feature of the acoustic radiation field is the polar extinction angles, that is, the region where there is zero sound emission. If we assume a perfectly axisymmetric quadrupole radiation field, the polar angles of extinction would lie exactly at 54.7 and 125.3 deg. However, direct simulations by Mitchell et al.[2] and Eldredge et al.[13] have revealed that the polar extinction angles from an axisymmetric vortex ring pairing are biased toward the upstream direction.

It is clear that several solution methods exist which can be used to predict the aeroacoustic phenomena. The MAE technique is limited to classical flow scenarios, and the solution field is only valid at $Ma \to 0$. Aeroacoustic theories such as Lighthill's[14] acoustic analogy and Powell's[1] vortex sound theory rely on the assumption of

Received 28 November 2003; revision received 3 September 2004; accepted for publication 18 September 2004.

*Research Student, Fluids Laboratory for Aeronautical and Industrial Research, Department of Mechanical Engineering.

†Associate Professor, Fluids Laboratory for Aeronautical and Industrial Research, Department of Mechanical Engineering.

‡Professor, Fluids Laboratory for Aeronautical and Industrial Research, Department of Mechanical Engineering. Member AIAA.

flow compactness and as such are restricted to low-Mach-number situations. On the other hand, full compressible flow computations are capable of computing the sound field and flowfield simultaneously without having to rely on those assumptions, but come at a significant cost compared to the other two solution methods.

This study is not seeking to justify Powell's theory of vortex sound via a numerical approach. Rather, we are adopting Powell's acoustic theory as a tool for gaining further understanding into the relationship between vorticity and sound generation in viscous flow phenomena. This study considers the effect of the initially identical toroidal ring radii on the acoustic radiation properties. The acoustic simulations are performed at a range of Mach numbers, which implies different levels of compactness for the two flow aspect ratios modeled. The simulations are compared with the predictions obtained through the method of MAE. The results of this study have indicated that the variations in the acoustic properties from the MAE predictions are strongly influenced by the viscous dynamics of the vortex core. An analysis of the effect of source compactness (synonymous with the low-Mach-number assumption) is examined through performing a decomposition of the predicted acoustic signals into a multipole expansion. Finally, the temporal behavior of the mathematical acoustic sources based on Kambe[12] is analyzed.

To be able to numerically predict the aerodynamic sound generation accurately, there are several issues that have to be considered. These issues are caused by the disparities in the flow energy and the acoustic energy and are rarely encountered in typical aerodynamic computations. For detailed information on the numerical issues associated with computational aeroacoustics, the interested reader can refer to, among others, Crighton,[15] Wells and Renaut,[16] and Tam.[17] The numerical techniques developed in this study tackle some of those issues in order to produce an acoustic solution without any artificial dissipation or explicit filtering scheme being used. The robustness of our two-step numerical procedure has been clearly demonstrated in an earlier study on the sound generated by an isolated corotating vortex pair.[4]

The layout of this paper is as follows. The numerical procedure of the two-step aeroacoustic prediction method is detailed in Sec. II. In Sec. III, the results of the flow simulations are presented followed by the acoustic simulations. The acoustic quantities are compared with the analytical predictions obtained using the method of MAE. Next, further analysis is performed on the predicted acoustic field. The procedure for the decomposition of the acoustic signals into a multipole expansion is summarized in Sec. III. The far-field directivity of the acoustic signals as the Mach number is varied is also discussed. Finally, concluding remarks to this study are offered.

II. Numerical Methodology

A. Flow Modeling Issues

The fluid is assumed to be incompressible and Newtonian, whereas the motion of the rings is assumed to be axisymmetric with no swirl component. A schematic of the flow problem is shown in Fig. 1. The symbols L and T denote the initially leading and trailing vortex cores. Both vortex rings have a toroidal ring radius y_0 and are initially separated in the axial direction by a distance of z_0. The azimuthal vorticity distribution of the core of each ring $\omega(r_c)$

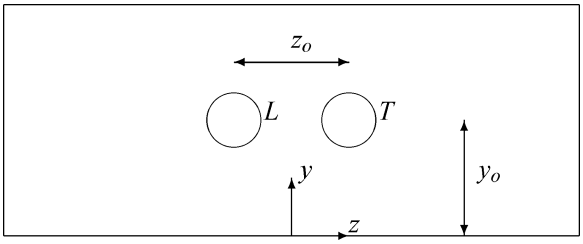

Fig. 1 Schematic of flow configuration of a pair of initially circular coaxial vortex rings. The symbol *y* represents the radial axis while the axial axis is represented by *z*.

Table 1 Spatial parameters of the flow configuration for the two cases considered

Case	e_0/z_0	e_0/y_0	z_0/y_0
1	0.075	0.0225	0.3
2	0.075	0.0375	0.5

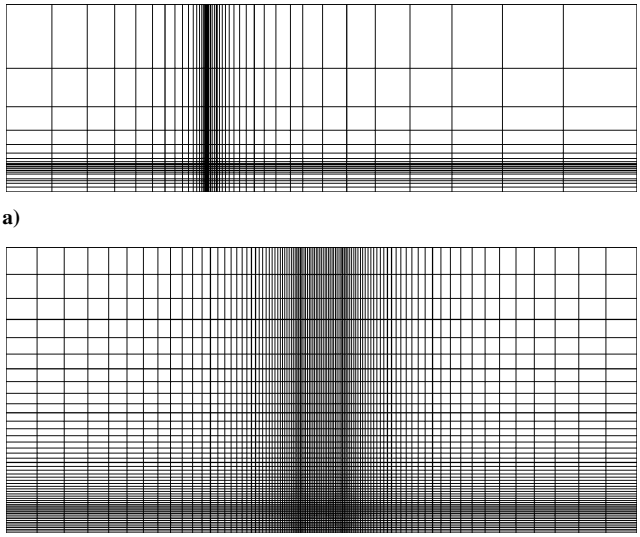

a)

b)

Fig. 2 Typical meshes used in the a) flow simulation and b) acoustic simulation. Note that the meshes have different scales. The vortex rings are initially located at the center of both computational domains.

is represented by a Gaussian function as follows:

$$\omega(r_c) = \frac{1.2495\Gamma_0}{\pi e_0^2} \exp\left[-1.25\left(\frac{r_c}{e_0}\right)^2\right] \tag{1}$$

where r_c is the polar radius from the center of the vortex core and e_0 is the thickness of the vortex core. This particular Gaussian distribution is identical to the one used by Mitchell et al.[2] and has been adopted by the present authors in an earlier study.[4] The Reynolds number is based on the circulation of the vortex core Γ_0 and is defined as $Re = \rho_0\Gamma_0/\mu_0 = 7500$.

Two cases are considered in this study. The spatial parameters of the flow configuration are reported in Table 1. As this study considers the effect of the initial ring toroidal radii, the other vortex ring parameters e_0 and z_0 are fixed. Therefore, the term (e_0/z_0), which represents the ratio of the core thickness to initial axial separation of the vortex rings, is constant. It is clear from Table 1 that both (e_0/z_0) and (e_0/y_0) are approximately one order of magnitude smaller than (z_0/y_0). This implies that the core of the vortex ring is "small" relative to its toroidal radius.

The incompressible Navier–Stokes equations, expressed in the cylindrical coordinate system, are solved using the finite volume method. Both spatial and temporal schemes are second-order accurate. The computational-fluid dynamics (CFD) domain is discretized into a structured mesh (shown in Fig. 2). It is clear that the grid is concentrated particularly in the region where the vortex rings are leap-frogging over each other as the entire vortex system is convecting in the downstream direction. To prevent a "checkerboard" pressure field, the velocity components and pressure are calculated on a staggered grid. At $y = 0$, the spatial derivatives in the flow equations are discretized without any special treatment owing to the staggered grid and the axisymmetric assumption. With regard to the boundary conditions, the axisymmetric condition is imposed at $y = 0$, while the pressure outlet condition is applied to all of the other boundaries. The solution field is initialized with the summation of the velocity distributions of each vortex core.

It is clear from Fig. 2 that the CFD domain has a rectangular shape that is biased toward the $+ve$ z direction. The dimensions

of the domain are as follows: $\{-5y_0 : 10y_0\}$ axially and $\{0 : 5y_0\}$ radially. The positive axial length at $10y_0$ is larger relative to the other directions because the domain has to be extended in order to capture the flow motion, that is, from leapfrogging to the final coalesence/merger of the vortex rings. The other lengths at $5y_0$ is deemed far away enough from the system that the motion of the rings is not affected by any artificial blockage effects.

Spatial and temporal resolution studies were carried out in order to ensure that the solution field is well resolved and the physics of the flow are accurately captured. For instance, the spreading of the vortex core must be a feature of the flow and not be accelerated because of excessive numerical dissipation. The peak vorticity was used to monitor flow convergence, and a tolerance level of 2% was used as the criteria to deem that the solution field is converged.

In the near field, the grid spacing is $\Delta x/e_0 = 0.1$, which places approximately 20 points across each vortex core. A linear stretching function is used in the mesh. To ensure that the flow is well resolved, that is, the spreading of the vortex core is caused by physical viscosity and not numerical dissipation, different rates of stretching were tested in the downstream direction. By comparing the peak vorticity, it was found that a stretching rate of 1.2% accurately captured the physics of the rings' motion. In contrast to the gradual stretching rate of 1.2% in the positive axial direction, the stretching applied in the other directions was set at 5%. From the temporal resolution studies, we found that the time step of $\Delta t u_0/y_0 = 3.98 \times 10^{-5}$ for $z_0/y_0 = 0.3$ and $\Delta t u_0/y_0 = 1.11 \times 10^{-4}$ for $z_0/y_0 = 0.5$ satisfied our convergence criteria.

B. Acoustic Modeling Issues

The governing equation for the far-field acoustic waves in an ambient medium according to Powell[1] (hereinafter known as the acoustic-wave equation) is as follows:

$$\frac{\partial^2 p}{\partial t^2} - c_0^2 \nabla^2 p = \nabla \cdot (\omega \times \boldsymbol{u}) \tag{2}$$

where p is the normalized acoustic pressure, c_0 is the wave propagation speed, and $\nabla \cdot (\omega \times \boldsymbol{u})$ is the acoustic forcing. As a matter of interest, the sound source is confined to the rotational part of the flow. The Mach number that is used in this study is defined as $Ma = u_0/c_0$, where $u_0 = [\Gamma_0/(4\pi y_0)][\log(8y_0/e_0) - \frac{1}{4}]$ is the translational velocity of the vortex ring in isolation.[18] The peak velocity of the vortex core at $r_c = e_0$ is not used as a reference velocity scale because the principal source of the acoustic radiation is from the induced motion of the rings.

The acoustic-wave equation is solved using the finite difference method. The spatial terms are discretized using the Taylor-series expansion, and the scheme is sixth-order accurate. A central-difference stencil is used as upwind schemes have been shown to be unstable in modeling the propagation of waves. Temporal marching of the acoustic-wave equation is performed using the fourth-order Runge–Kutta scheme. The relatively high-order spatial and temporal schemes are essential in order to minimize any artificial dispersion and dissipation errors induced by the truncation errors of lower-order schemes.

The radiation boundary condition of Bayliss and Turkel[19] is imposed on all external boundaries of the domain. The spatial stencil in the interior region consists of six nodes; hence, there are three ghost points on each external boundary. At $y = 0$, similar to the flow, periodicity of the acoustic field is also assumed. As such, the reflecting boundary condition is implemented at $y = 0$.

The acoustic domain is of a square shape and extends two wavelengths away. Similar to the CFD domain, it is discretized into a structured mesh (see Fig. 2). In the near-field region, the grid spacing is $\Delta x/e_0 = 0.45$ while the far-field grid spacing is $\Delta x/\lambda = 0.05$ (or $k\Delta x = 0.31$), which places 20 points across the acoustic wavelength. A nonuniform mesh is used in the domain as it would be too expensive otherwise. A linear stretching function is used to stretch the grid from the near field to the far field. A low grid-stretching rate is essential to ensure that the waves propagate smoothly throughout the domain without creating any spurious noise. Three different stretching ratios (2, 3, and 4%) were tested on the acoustic simulation at the lowest Mach number. This is because the acoustic signals at this particular Mach number are weakest and, hence, are most susceptible to any possible noise sources arising from errors induced as waves pass through the stretched grid or from initial transients. As the signal-to-noise ratio was good for both the two latter stretching ratios, the 3% stretching ratio was used in all subsequent acoustic simulations. To maintain a uniform rate of stretching at all Mach numbers, the total number of grid points in the computational aeroacoustics (CAA) domain are varied accordingly for each Mach number simulated.

To calculate the acoustic forcing, the hydrodynamic velocity components are interpolated in space and time from the CFD solution field to the CAA grid. There are two important things to note. Firstly, the distribution of the mesh points in both grids is different. Second, the time step used to advance the acoustic simulations is typically much smaller than that used in the flow simulations. This is because the time step in the acoustic computations is scaled to the sound speed c_0.

A second-order polynomial function is used in the spatial interpolation routine. This is because we want to maintain the same spatial accuracy as the flow solver. As the acoustic wavelength corresponds to the fundamental flow period, the spatial interpolation routine need not be carried out at every flow time step. A preprocessing task of determining the relevant number of frames per flow period that is needed to resolve the acoustic forcing as a function of time was conducted. Note that a fourth-order spline is used to interpolate the local values of the hydrodynamic components at the acoustic time step (which lies between the frames). The spline is relatively high order as it has been found that periodic kinks in the acoustic solution field would occur had a low-order function been used instead. The three different frames/period rates tested were 8, 16, and 24. Preliminary results indicated that there was little difference in the acoustic properties between the latter two frames/period rates. This implies that the temporal evolution of the acoustic source is well represented by a rate of 16 frames/flow period. It is clear that the effect of the higher-frequency component (associated with the vortex core deformation) would be filtered out when the nominated frame/period rate is used. This will be discussed in greater detail in Sec. III.B, where the acoustic results are reported.

Under the MAE framework, the vortex system is assumed to be radiating sound from a stationary position. Thus, in order to be able to compare our numerical results with the MAE-derived acoustic predictions, the convective velocity component of the vortex system must be removed prior to calculating the acoustic forcing. This would effectively peg the vortex system into its original position. As such, the acoustic source would be radiating sound from a fixed spatial location. To remove the convective velocity term, the translational velocity of the mean position of the vortex system is subtracted from the axial-velocity component. The instantaneous translational-velocity component is obtained by first fitting a third-order polynomial to the trajectory of the mean axial position of the vortex system over the entire flow evolution, followed by differentiating the function with respect to time to obtain the expression for the velocity. This procedure is carried out as a preprocessing step prior to the execution of the acoustic solver.

In computational aeroacoustics simulations, it is common knowledge that a poorly specified initial condition for the acoustic source terms would result in transient waves being created. As these waves propagate through the grid, high-frequency spurious waves are formed. Therefore in order to remove these contaminating waves, filtering schemes or artificial dissipation routines have to be used. Initial acoustic transient behavior has been observed in various aeroacoustic computations (for instance, see Lee and Koo[20] and Mitchell et al.[2]).

In this study, the effect of the initial transients on the acoustic solution field is largely minimized by using a startup function that introduces the acoustic source temporally. The acoustic forcing term $\nabla \cdot (\omega \times \boldsymbol{u})$ is multiplied by the startup function at every time step. The startup function is zero when the solution is initialized and increases gradually and smoothly to unity over a time interval t_r. Thus,

the purpose of the startup function is to prevent the initial transient from creating spurious noise, as it is well known that high-frequency, sharp transients would result in spurious grid-to-grid oscillations.

Through a series of tests with different t_r values ranging from zero to two periods, we found that a startup time interval of $t_r u_0/y_0 = 0.0597$ for $z_0/y_0 = 0.3$ and $t_r u_0/y_0 = 0.166$ for $z_0/y_0 = 0.5$ effectively resulted in an initial wave transient having similar timescale and amplitude to the acoustic signals. The ramping function was chosen as a quintic polynomial in time with the coefficients chosen to satisfy continuity of the function and the first and second derivatives at the endpoints. This meant that during the evolution, the transient could propagate out of the domain without leaving a sizable remnant field from the effects of imperfect transmission through the radiation boundary and passage through the stretched grid.

III. Results and Discussion

A. Flow Dynamics

Throughout the flow computation, the total circulation of the flow was constantly monitored and found to remain within 1% of its initial value. This implies that both the total circulation and impulse of the vortex system are conserved to numerical accuracy, that is, there are no external forces acting on the vortex system, and energy leakage from numerical inaccuracies is minimal. The circulation of the vortex rings is positive, that is, the rotation associated with each vortex core is anticlockwise. As such, the vortex system moves from the left to the right. In this study, the spatial positions of the peak vorticity are used to represent the centroids of the vortex cores. The axial trajectories of the initially leading and trailing core centroids are revealed in Figs. 3a and 3b. It is clear that the vortex system advects a considerable distance axially. For $z_0/y_0 = 0.3$, there were eight slip-through instants prior to the merging of the vortex rings. In contrast, there were seven slip-through instants for $z_0/y_0 = 0.5$. Here, the slip-through instant is defined as the time instant when both rings are furthest apart from each other radially. Thus, given a particular Reynolds number, the number of possible slip-through instants prior to the vortex rings merging is dependent on the aspect ratio z_0/y_0. It is clear that the number of slip-through instants would increase with a decreasing aspect ratio because the strength of the mutual induction of the vortex rings is increasing at the decreasing aspect ratio.

The period of the first leapfrogging cycle shown in Table 2 is estimated from the trajectories of the core centroids. During the initial stage of the interaction, there is excellent agreement with the predicted period from the analytical model. However, as the interaction continues, subsequent periods decrease as dissipation acts to diffuse the vortex cores, thereby allowing a more complex fluid dynamical interaction to occur. Figure 4a shows the change in the magnitude of the peak vorticity for each vortex ring over the entire flow evolution for the aspect ratio $z_0/y_0 = 0.3$. Between $tu_0/y_0 = 0$ and 0.13, representing a full period, there was a rapid decrease in peak vorticity with a drop in magnitude over the period of approximately 73% as the vortex cores rapidly diffuse. For $tu_0/y_0 > 0.13$, the rate of change of the peak vorticity becomes more gradual. For the aspect ratio $z_0/y_0 = 0.5$, between $tu_0/y_0 = 0$ and 0.32 (approximately one corotation period), the drop in peak vorticity was approximately 70% (Fig. 4b). The fact that the rate of vorticity diffusion at $z_0/y_0 = 0.5$ is similar to $z_0/y_0 = 0.3$ is expected because

Table 2 Tabulation of the first slip-through period

z_0/y_0	0.3	0.5
$T(u_0/y_0)$	1.03	2.433
$T(u_0/y_0)$[a]	0.997	2.129

[a]The values designated with an asterisk refers to classical vortex pairing interaction.

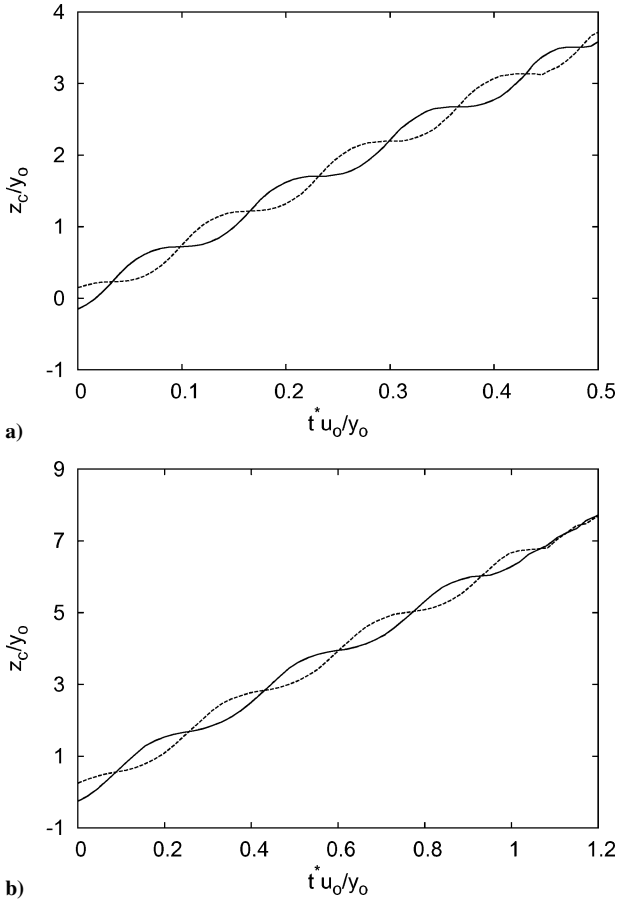

Fig. 3 Time traces of the axial trajectories of the initially leading and trailing core centroids. Here a) $z_0/y_0 = 0.3$ and b) $z_0/y_0 = 0.5$: ——, initially leading and – – –, initially trailing.

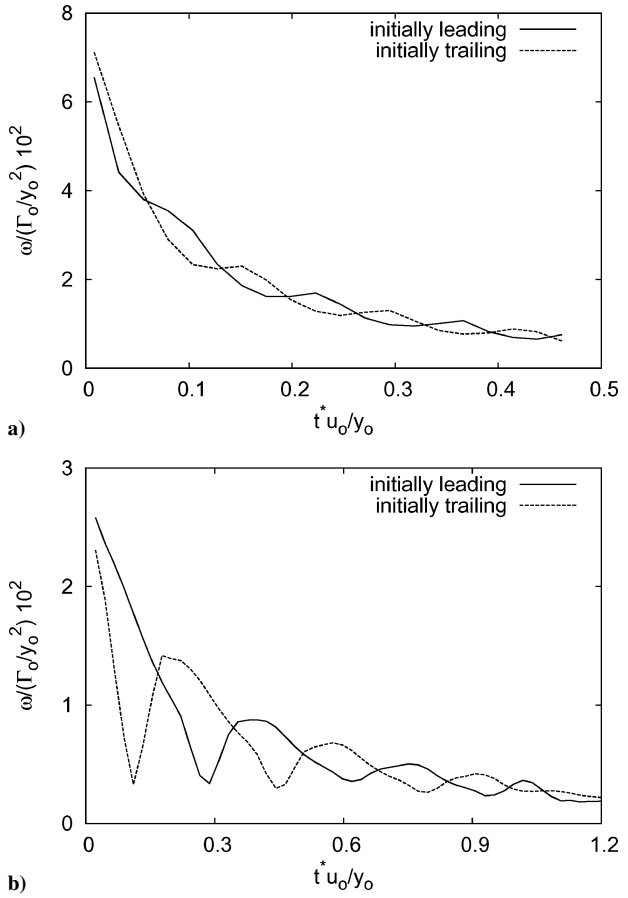

Fig. 4 Time traces of the peak vorticity of the initially leading- and trailing-core centroids. Here, z_0/y_0 = a) 0.3 and b) 0.5.

the initial vorticity distribution of the vortex cores and the Reynolds numbers are identical. Another point of interest is that the difference in the peak vorticity between the rings is greatest at the slip-through instant. Conversely, when the axial distance separating the vortex cores is a maximum the peak vorticities of the two cores are virtually identical. In the classical model, the interactions of the vortex rings are "elastic." While the initially leading vortex ring contracts and accelerates axially toward the slip-through position, its counterpart, being the initially trailing vortex ring, expands and decelerates axially. As soon as the slip-through position is reached, the roles of the vortices are reversed. The interactions of the viscous rings simulated in this study are expected to differ from the classical model.

For $z_0/y_0 = 0.3$, the interaction of the rings through the first half of the leapfrogging cycle is shown through the series of vorticity contours in Figs. 5. The contours are recorded between simulation times of $tu_0/y_0 = 0.13$ and 0.194. The first snapshot shown in Fig. 5 corresponds approximately to the instant of maximum axial separation. Note that the contours are not shown from the start of the start of the flow simulation because during the initial stages there is an adjustment as the flow evolves from the initially imposed velocity field. Figures 6 show the corresponding vorticity snapshots for $z_0/y_0 = 0.5$ taken between $tu_0/y_0 = 0.328$ and 0.492. It is clear that the distortion of the vortex rings increases with aspect ratio z_0/y_0.

Figures 7 and 8 shows the vorticity contours during the merging process for the two aspect ratios. In contrast to the passage interactions, the vortex merger process is characterized by large core deformations. As the vortex core deforms and assumes an elliptical shape, the tip starts to a form a fine-scale low-vorticity filament. This is known as the filamentation process. It is also clear that the spatially thin filament structures are not as well resolved as the initially circular vortex cores. The rings gradually wrap around each other, and when they are sufficiently close to each other they become intertwined. This occurs at approximately at the final slip-through instant. The vortex merger/coalescence process occurs over a relatively short time interval, about half that of the leapfrogging period. Although the fine-scale structure of the vortex filaments are not the dominant sound sources, it has been shown in many investigations (for instance, Melander et al.[21]) to be crucial to the merging process.

B. Propagation and Decay of the Acoustic Waves

This section presents the results of the acoustic simulations of both aspect ratio $z_0/y_0 = 0.3$ and 0.5. The simulations were performed at three different Mach numbers: $z_0/y_0 = 0.3$, $Ma = \{1.4^{-2}, 2.8^{-2}, \text{and } 5.6^{-2}\}$, $z_0/y_0 = 0.5$, $Ma = \{1.3^{-2}, 2.6^{-2}, \text{and } 5.2^{-2}\}$. Owing to the symmetry of the flow motion, this implies that the acoustic wavelength is defined as $\lambda = c_0 T/2$. At the Mach numbers considered, the disparity in the acoustic wavelength and the flow characteristic length scale is as follows: for $z_0/y_0 = 0.3$, $\lambda/y_0 = \{6.5, 13, 26\}$, and for $z_0/y_0 = 0.5$, $\lambda/y_0 = \{16.4, 32.8, 65.6\}$. The relatively large spread of length-scale ratios enables us to access the applicability of Powell's[1] theory of vortex sound as it rests on the crucial assumption that flow is compact, that is, $\lambda \gg y_0$. This will be discussed in greater detail in the multipole analysis of the acoustic signals.

The time history of the pressure fluctuations at $r = 0.5\lambda$ (where r is the radial distance from the reference axes) is shown in Fig. 9. The variations in pressure are shown against retarded time, represented by the symbol t^*. It is clear that there is a significant difference in the mean of the pressure fluctuations when compared to the MAE theoretical predictions (which are shown in Fig. 10). This suggests that at $r = 0.5\lambda$ the pressure fluctuations are affected by the spatial distribution of the acoustic source. However, it is expected that the effect of the source distribution would reduce as the observation position is moved further away. Our results show that the mean of the pressure fluctuations decreases as a function of the radial distance and converges to a constant state for points located at $r \geq 1.5\lambda$. This implies that at $r \geq 1.5\lambda$ the pressure fluctuations are effectively far-field acoustic signals, as the fluctuations are caused primarily by the temporal variation of the acoustic source rather than by its spatial distribution. Because the pressure signals were virtually identical in form at the different far-field positions, only the pressure–time histories for $r = 2\lambda$ are shown (see Fig. 11).

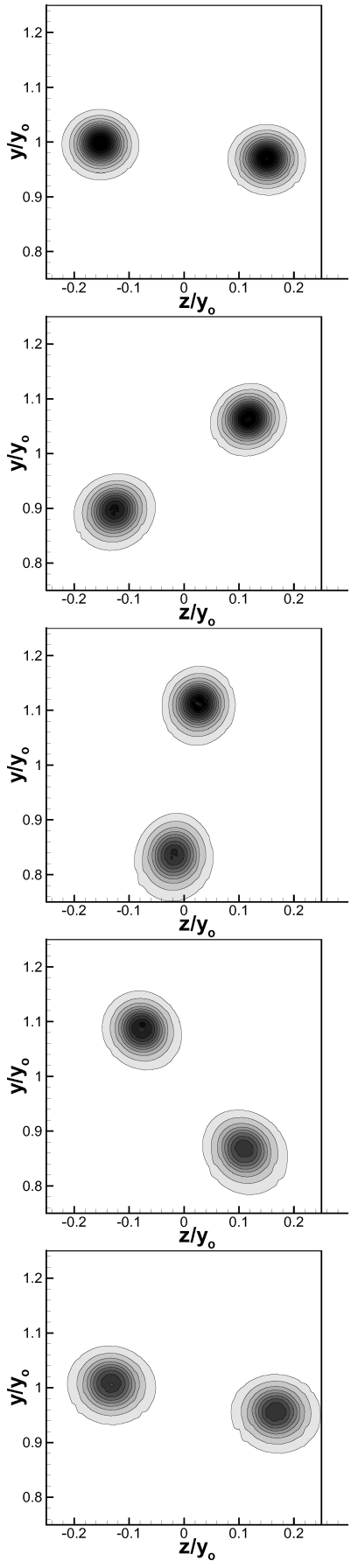

Fig. 5 Instantaneous contours of vorticity for $z_0/y_0 = 0.3$. From top to bottom: $tu_0/y_0 = 0, 0.13, 0.146, 0.162, 0.178$, and 0.194. The contour levels are $\omega_{max}/\omega_0 = 0.224$ and $\Delta\omega = 0.0025$. Note that ω_0 represents the peak vorticity of core.

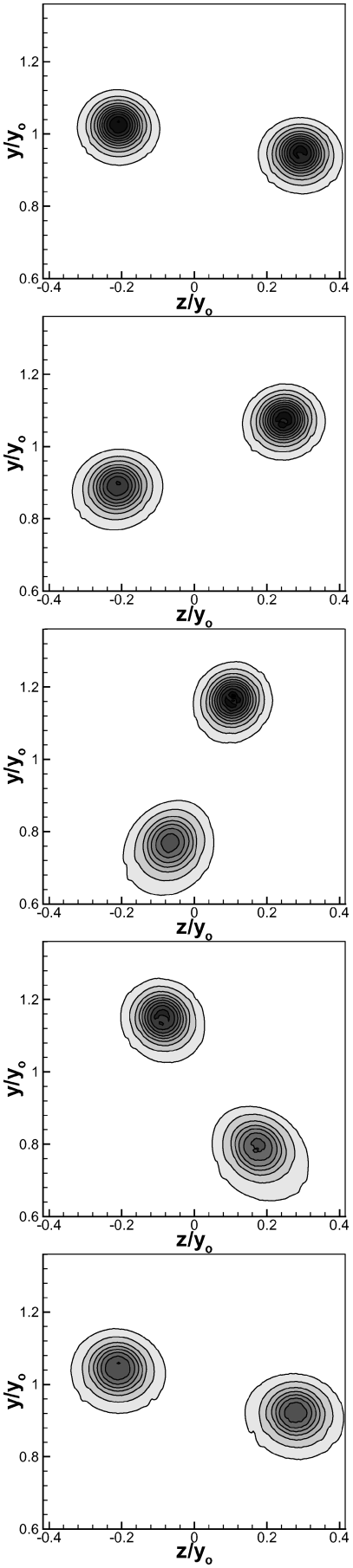

Fig. 6 Instantaneous contours of vorticity for $z_0/y_0 = 0.5$. From top to bottom: $tu_0/y_0 = 0$, 0.328, 0.368, 0.409, 0.451, and 0.492. The contour levels are $\omega_{max}/\omega_0 = 0.305$ and $\Delta\omega = 0.003$.

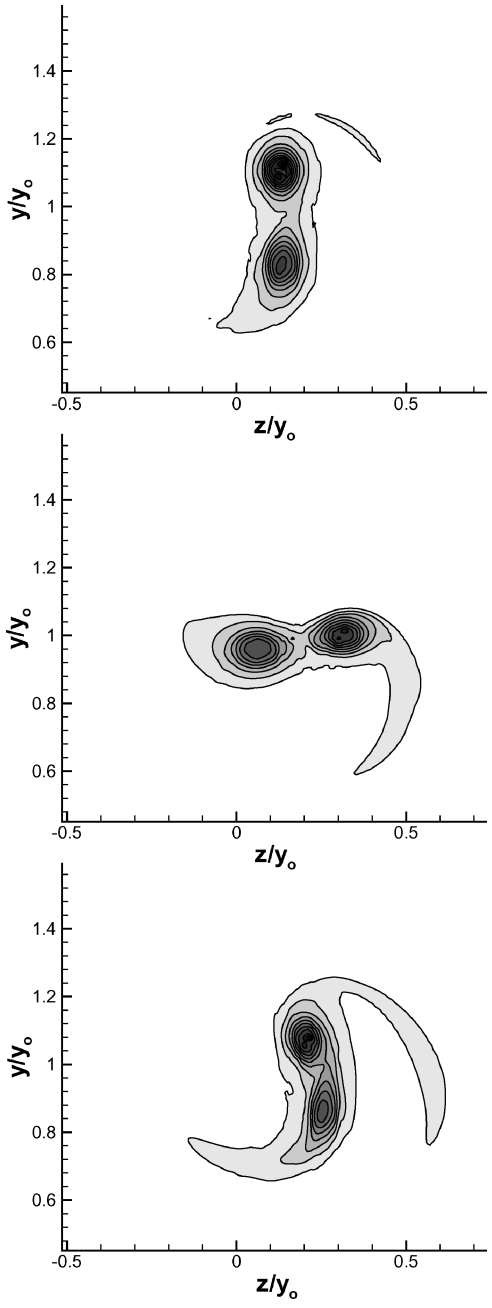

Fig. 7 Snapshots of vorticity prior to merging: $z_0/y_0 = 0.3$. From top to bottom: $tu_0/y_0 = 0.43$, 0.462, and 0.486. The contour levels are $\omega_{max}/\omega_0 = 0.204$ and $\Delta\omega = 0.002$.

The acoustic signals recorded on the axial axis are out of phase by 180 deg with those on the radial axis. The phase change of the acoustic signal, or line of nodes, occurs along a radial line at a specific angle known as the polar extinction angle. Although the time variation of the pressure trace from an isolated two-dimensional vortex pair shows an approximately sinusoidal pattern,[2,4] in the present study the effect of axisymmetry means the acoustic oscillations consist of a series of sharper peaks and broader troughs. Note that the number of peaks found for each aspect ratio corresponds to the number of slip-through instants. Figures 9 and 11 shows pressure traces at different observation positions. The first part of the signal, for approximately half of a leap-frogging cycle, is affected by the initial startup function. The gradual introduction of the acoustic source through the use of the startup function coupled with only gentle stretching of the grid meant that there were no obvious reflections as the initial transient propagated through the region of grid stretching. As seen in Figs. 9 and 11, the initial transient and

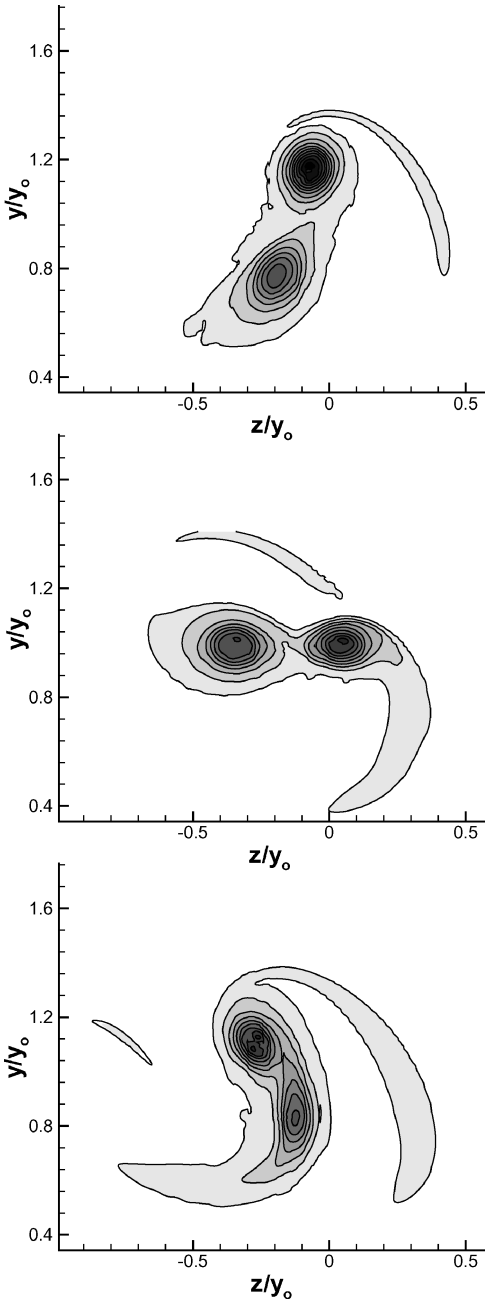

Fig. 8 Snapshots of vorticity prior to merging: $z_0/y_0 = 0.5$. From top to bottom: $tu_0/y_0 = 0.918$, 0.995, and 1.06. The contour levels are $\omega_{max}/\omega_0 = 0.204$ and $\Delta\omega = 0.002$.

subsequent acoustic peaks have comparable amplitude. Reducing the amplitude and increasing the timescale of the transient so that it is of the same order as the true acoustic signal, amplitude is sufficient to prevent the acoustic field at later times from being contaminated with significant residual noise.

Correlating the time histories of the acoustic pressure fluctuations with the trajectories of the core centroids, the occurrence of the acoustic peaks was found to correspond to the slip-through instants. This finding is consistent with the results of Kambe and Minota[6] and Tang and Ko.[10] The acoustic signals displayed a gradual increase in the amplitude and frequency of oscillations. This is because of the increase in the induced angular velocity to conserve angular momentum as the vortex rings start to move closer to each other. Furthermore, the largest acoustic peak was found to occur at the instant of the vortex merger.

Figure 12 shows the peak pressure associated with the second slip-through instant and located at $(r, \theta) = (2\lambda, 0 \text{ deg})$ plotted as a function of the Mach-number range simulated. We observe that the

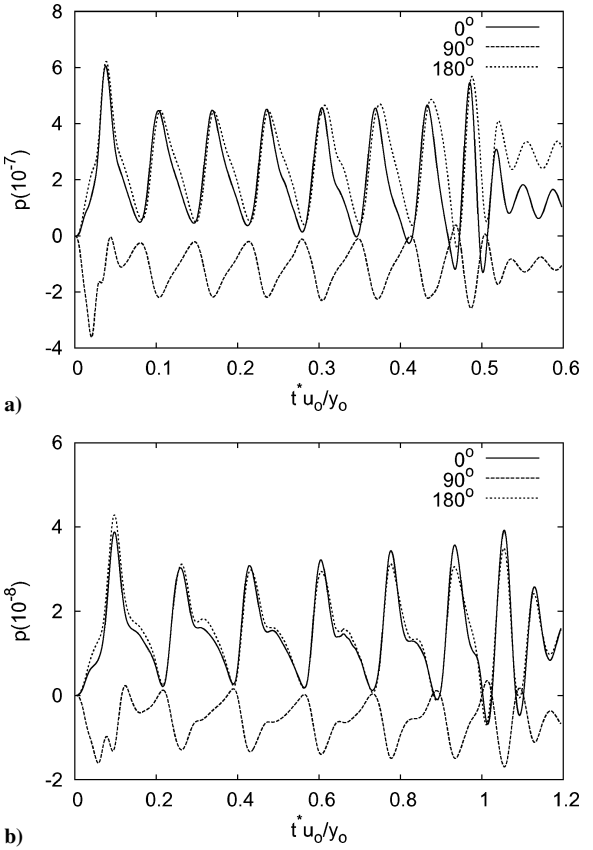

Fig. 9 Predicted time histories of the far-field acoustic pressure fluctuations at $r = 0.5\lambda$. Here, a) $z_0/y_0 = 0.3$, $Ma = 0.014$; and b) $z_0/y_0 = 0.5$, $Ma = 0.013$. The angles are measured anticlockwise from the positive z axis.

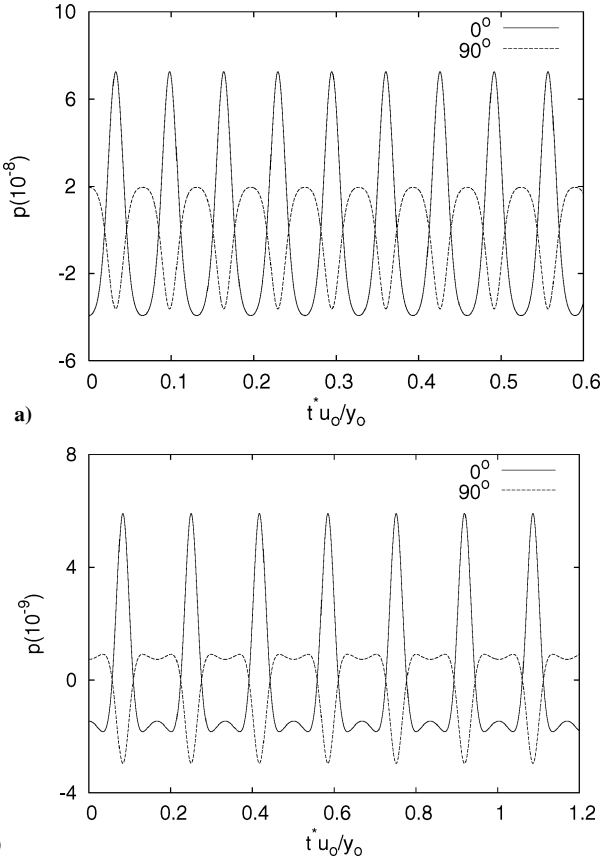

Fig. 10 Time histories of the acoustic pressure fluctuations (calculated using the MAE far-field expression) at $r = 2\lambda$. Here, a) $z_0/y_0 = 0.3$, $Ma = 0.014$; and b) $z_0/y_0 = 0.5$, $Ma = 0.013$.

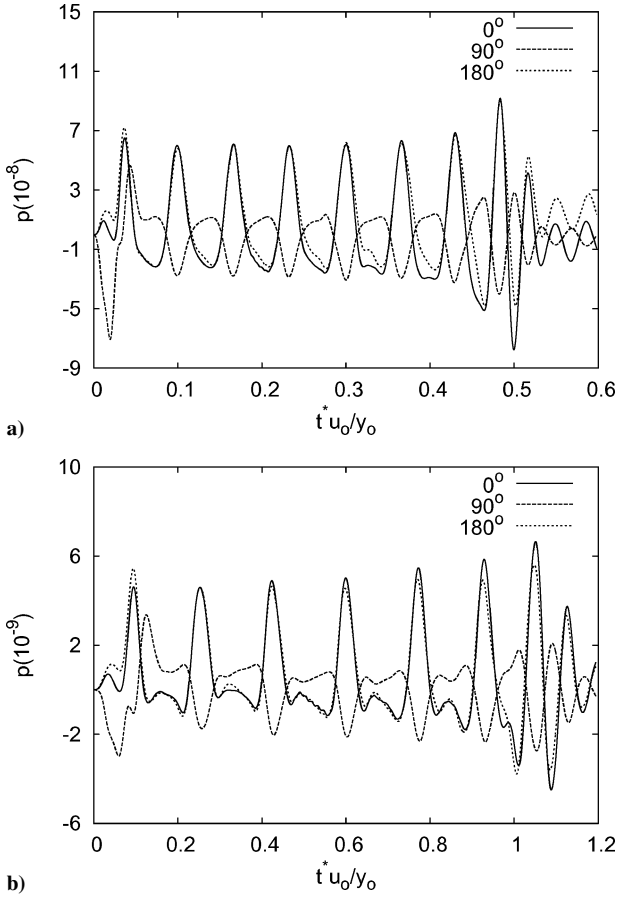

Fig. 11 Predicted time histories of the far-field acoustic pressure fluctuations at $r = 2\lambda$. Here, a) $z_0/y_0 = 0.3$, $Ma = 0.014$; and b) $z_0/y_0 = 0.5$, $Ma = 0.013$. The angles are measured anticlockwise from the positive z axis.

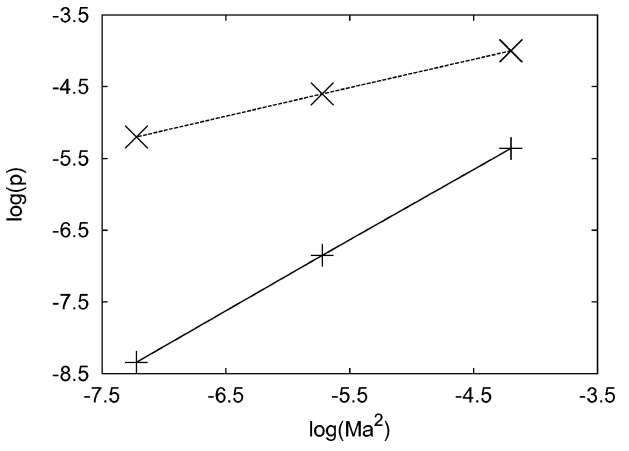

Fig. 12 Peak acoustic pressure (second slip-through) at $(r, \theta) = (2\lambda, 90$ deg) at the three different Mach numbers simulated: ×, $z_0/y_0 = 0.3$ and +, $z_0/y_0 = 0.5$.

acoustic pressure is proportional to the square of the Mach number. This relationship is in agreement with the MAE far-field expression.

Instantaneous pressure contours while the vortex system is still engaged in the leapfrogging motion are shown in Figs. 13 and 14. It is clear that the pairing of the vortex rings results in an axisymmetric lateral quadrupole. Comparing the contours for the two aspect ratios, it is also evident that at the lower aspect ratio the far field has a slightly greater amplitude in the upstream direction. The application of the MAE technique to the idealized axisymmetric point vortex model leads to the prediction that the amplitude and frequency of the acoustic signal remain constant as shown in Figs. 10. This is because the periodic leapfrogging motion repeats itself indefinitely. In

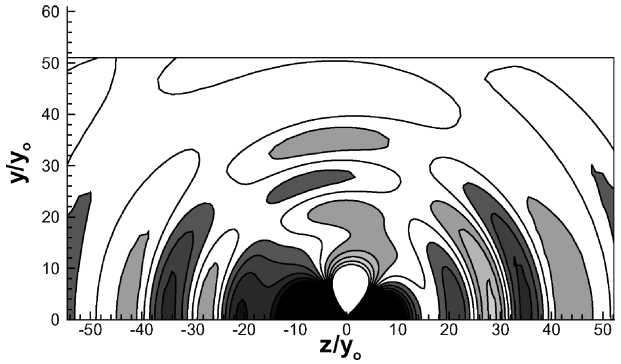

Fig. 13 Instantaneous contours of the acoustic pressure fluctuations at $t^* u_0/y_0 = 0.573$. Here, $(z_0/y_0) = 0.3$ while $Ma = 0.014$. The contour levels are $p_{\min} = -2 \times 10^{-7}$, $p_{\max} = 2 \times 10^{-7}$ and $\Delta p = 2 \times 10^{-8}$.

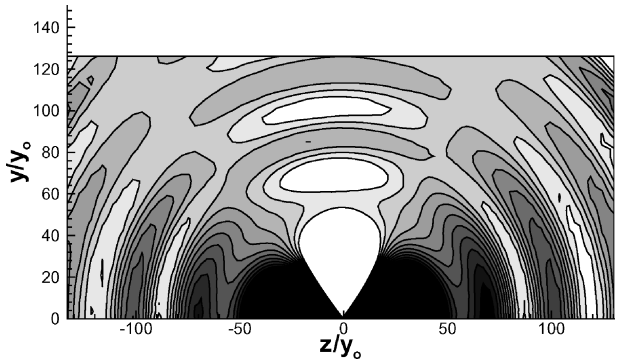

Fig. 14 Instantaneous contours of the acoustic pressure fluctuations at $t^* u_0/y_0 = 1.548$. Here, $(z_0/y_0) = 0.5$ while $Ma = 0.013$. The contour levels are $p_{\min} = -0.5 \times 10^{-9}$, $p_{\max} = 3 \times 10^{-9}$ and $\Delta p = 0.35 \times 10^{-9}$.

contrast, for the current model, Figs. 9 and 11 show that the signal is neither periodic nor of constant amplitude. The effects of finite core size, viscous diffusion, and vortex dynamics cause the amplitude of the predicted pressure traces to be slightly lower, although there is an increase in amplitude during the evolution, and the frequency increases gradually prior to vortex merger. The smaller amplitude, especially initially, can probably be attributed to the diffusion of the vortex cores during the evolution. Counteracting this effect is the increasing frequency as the vortices move toward merger, which in turn is associated with a growing amplitude of the pressure signal over a longer time span. Apart from the amplitude variation during the evolution, it is also clear that there are differences in the waveform of the signals, particularly at the troughs. Furthermore, the deviation from the analytical prediction increases with the aspect ratio z_0/y_0, and as such is attributed to the distortion of the vortex rings during the leapfrogging cycles.

One of the differences between our results and those of Shariff et al.[9] and Tang and Ko[10] is that there were no wavy oscillations found in our time histories of the acoustic pressure. Verzicco et al.[11] have suggested that the secondary frequency is related to the nutation of the vortex core. The nutation time is the time taken for a particle located at the point of maximum tangential velocity to orbit once around a vortex core. Because both cases have identical core thicknesses, the secondary frequency is identical for both aspect ratios. With the Gaussian vortex core model, the position of maximum tangential velocity is located at the core radius e_0. The secondary frequency was calculated to be approximately three orders of magnitude higher than the fundamental frequency. In this study, the reconstruction of the acoustic forcing by interpolation from a small number of samples and the arrangement of the grid points in the acoustic domain are geared toward resolving the acoustic solution at the fundamental frequency. As a result, the fact that no wavy oscillations were found in the present study should not be surprising. This issue also highlights one of the potential difficulties of numerically solving an acoustic problem with multiple sources at widely different frequencies.

C. Decomposition of the Acoustic Signals

One of the limitations of using the MAE technique to predict vortex-pairing induced sound is that the validity of the analytical far-field expression away from the asymptotic limit $Ma \to 0$ is unclear. Hence, in this study the influence of finite, nonzero Mach number on the far-field directivity is investigated through performing acoustic simulations for each aspect ratio z_0/y_0 at three different Mach numbers. The predicted acoustic signals are then decomposed into harmonic modes to quantify the contributions of each term. This analysis has been used previously by Inoue and Hatakeyama,[22] and it is possible because the acoustic waves are linear. The acoustic signal can be expressed as a sum of harmonic functions as follows:

$$p(z, y) = A_0(r) + \sum_m B_m(r)\cos(m\theta) \tag{3}$$

where $m = 1, 2, 3, \ldots$. The first term A_0 is the zeroth-order mode while $B_{m=1\ldots\infty}$ are the mth-order cosine modes. Note that there are no sine modes present in the expansion because of the assumption of axisymmetricity in the flow. The terms A_0 and B_m are given as follows:

$$A_0(r) = \frac{1}{2\pi}\int_0^\pi p(r, \theta)\,\mathrm{d}\theta$$

$$B_m(r) = \frac{1}{\pi}\int_0^\pi p(r, \theta)\cos(m\theta)\,\mathrm{d}\theta$$

The amplitudes of the harmonic modes from $m = 0$ to 3 for both cases are shown in Figs. 15a–15c and 16a–16c. Note that the contributions from modes greater than $m = 3$ are too small to be of any significance and as such are not included in the analysis. The values

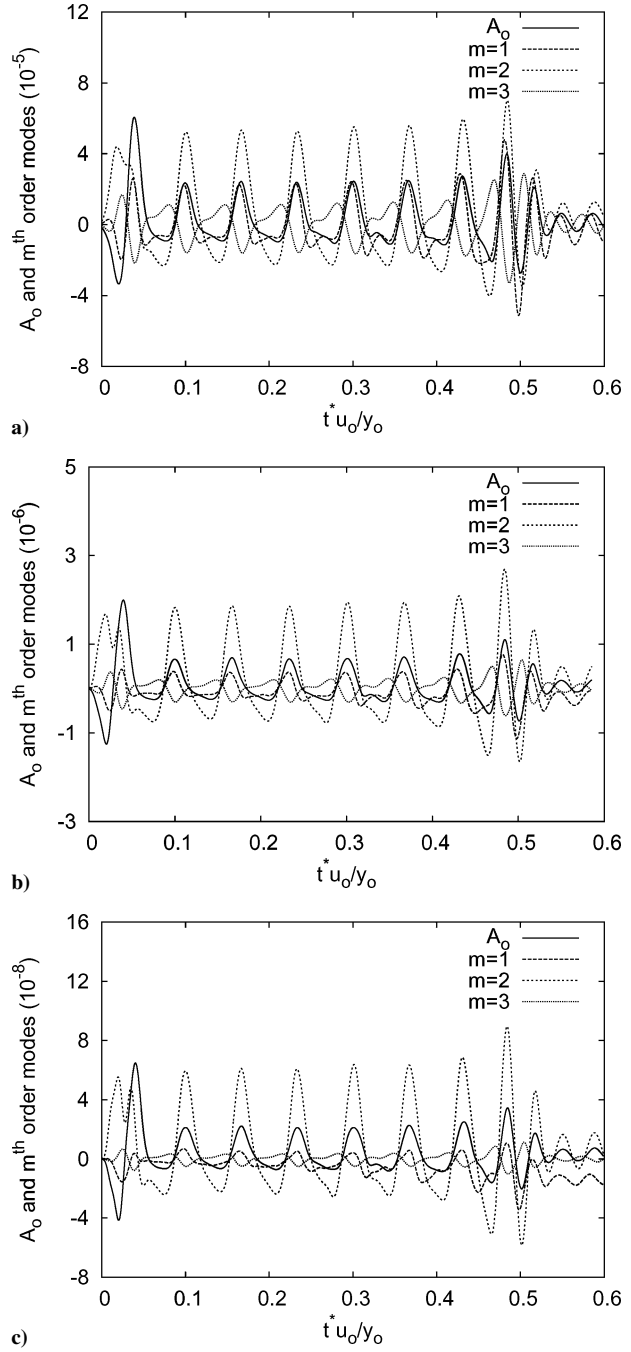

Fig. 15 Time histories of the amplitudes of A_0 and mth-order cosine modes. Here, the aspect ratio is $(z_0/y_0) = 0.3$. The three different Mach numbers are a) $Ma = 0.056$, b) 0.028, and c) 0.014.

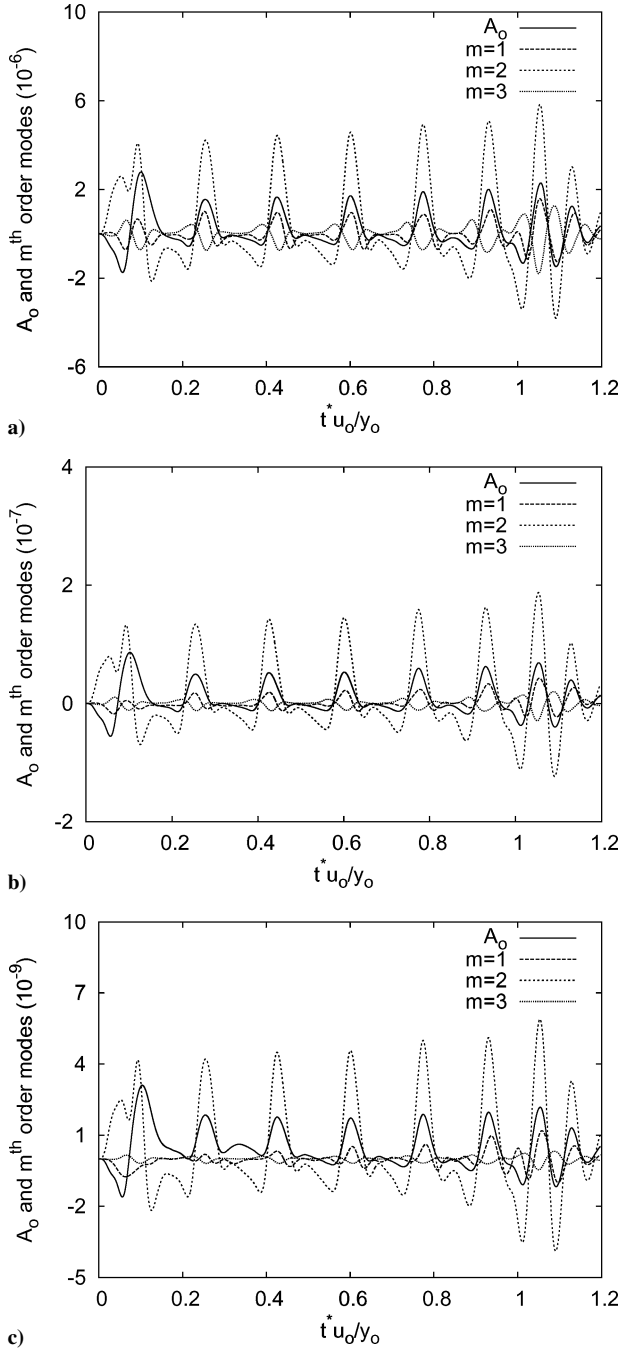

Fig. 16 Time histories of the amplitudes of A_0 and mth-order cosine modes. Here, the aspect ratio is $(z_0/y_0) = 0.5$. The three different Mach numbers are a) $Ma = 0.052$, b) 0.026, and c) 0.013.

of the harmonic modes were obtained by numerically integrating the pressure fluctuations along a semicircle at $r = 1.5\lambda$. Because the CAA grid is formed from quadrilateral cells, the bilinear method was used to interpolate the nodal values from the grid onto radial integration points. The integration method used was Simpson's $\frac{1}{3}$ rule with 50 increments over π. In the MAE analysis of a pair of interacting inviscid coaxial vortex rings, the spatial dependence of the far field is represented by the sum of a zeroth-order mode and a second-order cosine mode. In contrast, it is clear from Figs. 15 and 16 that finite Mach numbers result in other modes being present. In particular, as the source becomes less compact the amplitude of the first-order mode becomes comparable to the zeroth-order mode. This explains the shift in the polar extinction angles as a function of Mach number as discussed next.

Once the amplitudes of the harmonic modes are calculated, the contributions of the modes at the second slip-through instant can be used to determine the polar extinction angles. The acoustic pressure located at the polar extinction angles remains zero and is time invariant. To calculate the polar extinction angle, the sum of the harmonic modes is equated to zero, and the harmonic expression is then iterated numerically.

Table 3 Polar angles of extinction as a function of Mach number for both aspect ratios[a]

z_0/y_0	$Ma(10^{-2})$	1st deg	2nd deg
0.3	5.6	72.5	107.5
0.3	2.8	63.9	116.1
0.3	1.4	59.9	120.1
0.5	5.2	64.1	115.9
0.5	2.6	60.3	119.7
0.5	1.3	60.1	119.9

[a]The angles were calculated at the second slip-through instant.

The first and second polar angles of extinction, calculated at the second slip-through instant, are shown in Table 3. It is clear that as the Mach number is decreased the polar extinction angles approach the theoretical values for axisymmetric point quadrupoles of 54.7 and 125.3 deg. For aspect ratio $z_0/y_0 = 0.5$, there is very little variation in the polar extinction angles between $Ma = 0.013$ and 0.026, suggesting that the compact-source assumption is well satisfied. The "converged" numerical polar extinction angles deviate from the theoretical values by $\approx 10\%$. Plausible explanations for the cause of the deviation might be the effects of finite-core thickness and/or dynamics of the viscous core. This subject is currently being investigated by the authors of the present study.

In contrast to the larger aspect ratio, for aspect ratio $z_0/y_0 = 0.3$ there is still a significant change in the the polar extinction angles of the three Mach numbers modeled. Hence, it is not clear that the compact-source assumption have been fully met. This implies that further simulations would have to be performed at even lower Mach numbers in order to determine the threshold Mach number where the application of Powell's vortex sound theory is justified. This highlights one of the limitations of Powell's vortex sound theory. It is also clear that full direct numerical simulations would have to be used for scenarios, where the flow length scale and acoustic wavelength are comparable.

D. Analysis of the Quadrupole and Monopole Sound Sources

Kambe and Minota[6] and Kambe[12] used the MAE technique to study the acoustic radiation of axisymmetric flows with zero swirl component asymptotic expansions. They showed that the far-field acoustic signal is defined as follows:

$$p(z, y, t^*) = \frac{\rho_0}{4c_0^2\sqrt{(z^2+y^2)}}\frac{\partial^3 Q}{\partial t^3}\left(\cos^2\theta - \frac{1}{3}\right) + \left(\frac{5-3\gamma}{3}\right)\frac{\partial^2 K}{\partial t^2} \tag{4}$$

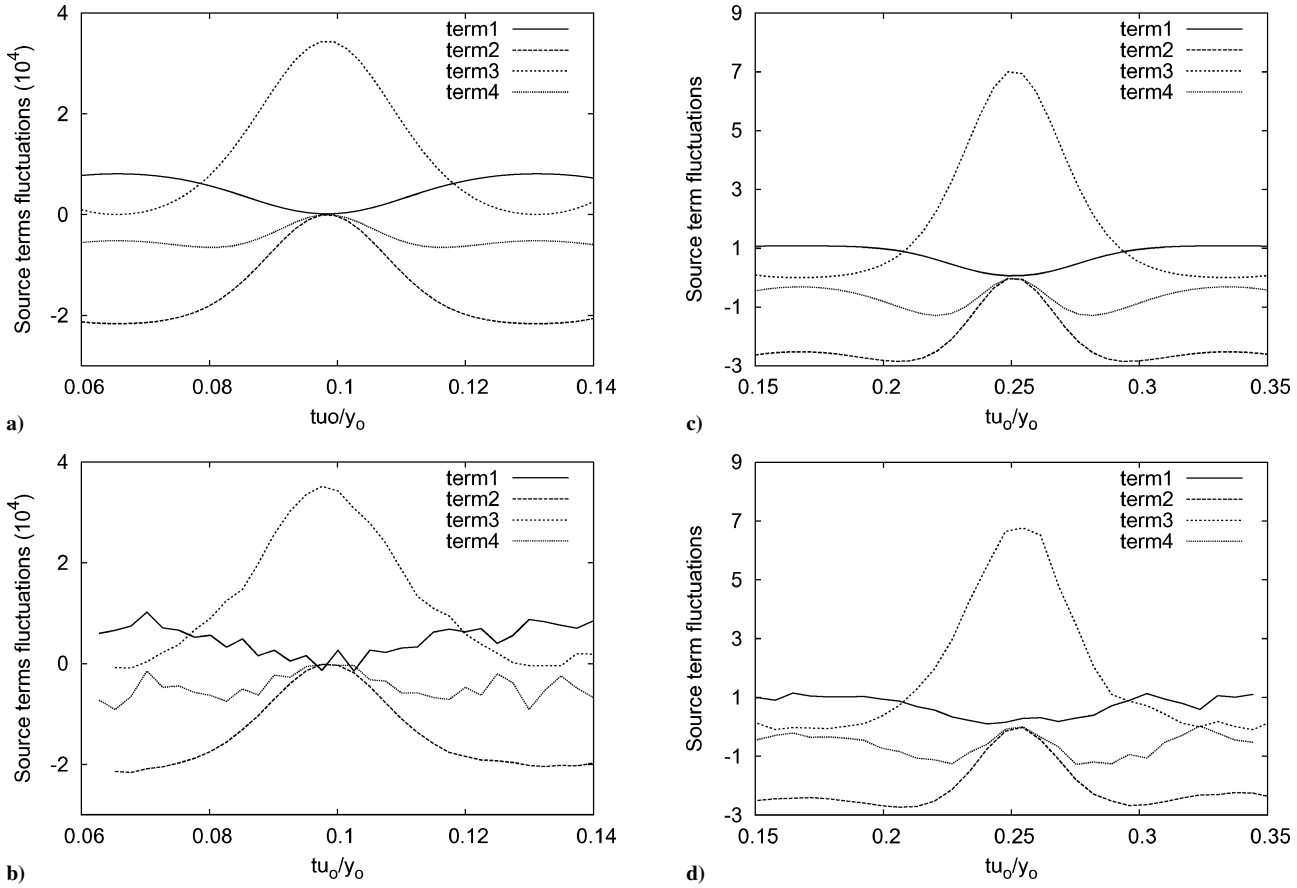

Fig. 17 Sample time trace of the four source terms as presented by Tang and Ko.[10] Term 1 is $\sum[I(\partial^3 z/\partial t^3)]$, term 2 is $3(\Delta\ddot{z})\dot{I}_l$, term 3 is $3(\Delta\dot{z})\ddot{I}_l$, and term 4 is $(\Delta z)(\partial^3 I_l/\partial t^3)$. The aspect ratio is $z_0/y_0 = 0.3$ for panels a and b and 0.5 for panels c and d. Here, panels a and c represent the classical model results, whereas panels b and d represent the results from the simulations.

where $\partial^3 Q/\partial t^3$ is classified as a quadrupole source term and $\partial^2 K/\partial t^2$ is described as a monopole source because of its respective far-field directivities. When the motion of the interacting vortex rings is derived using Dyson's[23] model, the quadrupole sound source has been shown by Kambe and Minota[6] to be related to the rate of change of the mean axial position of the vortex system. To further relate the quadrupole source mechanism in terms of the dynamics of the vortex rings, Tang and Ko[10] expanded on Kambe and Minota's[6] analysis and derived a formula for the quadrupole term as follows:

$$\frac{\partial^3 Q}{\partial t^3} = \sum \left(I \frac{\partial^3 z}{\partial t^3} \right) + 3(\Delta \ddot{z}) \dot{I}_L + 3(\Delta \dot{z}) \ddot{I}_L + (\Delta z) \frac{\partial^3 I_L}{\partial t^3} \quad (5)$$

Here the symbol Δ in the preceding equation represents the difference operator. The quadrupole term as defined by Tang and Ko[10] relates acoustic fluctuations in terms of the positions, velocities, and accelerations of the vortex cores in the axial direction and the impulses of the initially leading- and trailing-core centroids.

Comparison is made of the source terms as presented by Tang and Ko,[10] calculated using the classical model and the simulation data. Figure 17 shows a sample time trace of the four source terms. The time trace is representative of the leapfrogging motion prior to vortex merger because the trajectories of the core centroids are largely repeatable with only small changes caused by viscous dissipation. The source terms evaluated from the simulation data are compared with those calculated using the classical model of Dyson.[23] It is clear that the term $3(\Delta \dot{z}) \ddot{I}_l$ is the dominant term at the slip-through instant. This finding in consistent with Tang and Ko.[10] Also note that the kinks observed in Figs. 17b and 17d do not imply the presence of the secondary acoustic component. It is thought to be caused by the near-field grid spacing in the flow simulation leading to slight underresolution of high-order derivative terms such as the third-order time derivatives of the impulse and axial trajectory of the vortex cores. This is particularly true for the case with the larger aspect ratio, that is, smaller rings. The monopole source was also calculated along with the quadrupole sound source and was found to be approximately two orders of magnitude smaller than the latter. This is consistent with the findings of Verzicco et al.[11]

IV. Conclusions

A numerical study into the sound radiation from the mutual interaction of a pair of viscous axisymmetric coaxial vortex rings was performed. In particular, the effect of the initial toroidal ring radii was considered. Powell's[1] theory of vortex sound was used as the acoustic prediction tool. The secondary component (owing to the nutation of the vortex core) was not considered as it has been shown to be relatively insignificant compared to the fundamental component (leapfrogging cycle).

The results are in broad agreement with that of other investigators, that is, 1) that the far-field pressure signal is strongly associated with the leapfrogging motion of the vortex rings, 2) the amplitude and frequency of the acoustic signal increase gradually over successive leapfrogging cycles, and 3) the acoustic fluctuations reach a maximum at the instant of the merging of the vortices and decay rapidly thereafter.

Comparison of the numerical results with the matched asymptotic expansion (MAE) predictions yielded some interesting observations. First, the slight difference in the amplitude of the acoustic signal is attributed to the strong diffusion of the core vorticity, which occured during the initial stages of the flow. Second, the difference in the time variation of the acoustic signals (particularly at the troughs) is related to the distortion of the vortex cores caused by the inclusion of viscous effects and vortex dynamics of finite sized vortex cores. As the ratio z_0/y_0 is increased, the core distortion intensified leading to a greater deviation from the MAE predictions.

The effect of a finite Mach number was analyzed through a multipole expansion of the predicted acoustic field. Using the expansion relation, the location of the polar angles of extinction can be determined. We found that the numerical polar extinction angles deviated from the theoretical values by about 10%. This shift, which is suspected to be caused by the deformation of the core, is currently being investigated by the present authors.

The flow simulation data were to predict the quadrupole and monopole source terms. The method of analysis method is based on Kambe and Minota[6] and Kambe.[12] The dominant sound source was found to be the quadrupole. In contrast, the monopole caused by presence of viscosity was at least two orders of magnitude smaller.

Acknowledgments

The financial support from Monash University in the form of the Monash Graduate Scholarship and the International Postgraduate Research Scholarship is also acknowledged. Keith Liow expresses his gratitude to B. T. Tan for the many insightful discussions on the subject of aerodynamic sound generation.

References

[1]Powell, A., "Theory of Vortex Sound," *Journal of the Acoustical Society of America*, Vol. 36, No. 1, 1964, pp. 177–195.

[2]Mitchell, B. E., Lele, S. K., and Moin, P., "Direct Computation of the Sound from a Compressible Co-Rotating Vortex Pair," *Journal of Fluid Mechanics*, Vol. 285, 1995, pp. 181–202.

[3]Bridges, J., and Hussain, F., "Direct Evaluation of Aeroacoustic Theory in a Jet," *Journal of Fluid Mechanics*, Vol. 240, 1992, pp. 469–501.

[4]Liow, Y. S., Thompson, M. C., and Hourigan, K., "Computation of Acoustic Waves Generated by a Co-Rotating Vortex Pair," *14th Australasian Fluid Mechanics Conference*, edited by B. B. Dally, Vol. 1, Adelaide Univ., Adelaide, Australia, 2001, pp. 99–102.

[5]Möhring, W., "On Vortex Sound at Low Mach Number," *Journal of Fluid Mechanics*, Vol. 85, 1978, pp. 685–691.

[6]Kambe, T., and Minota, T., "Sound Radiation from Vortex Systems," *Journal of Sound and Vibration*, Vol. 74, No. 1, 1981, pp. 61–72.

[7]Lamb, H., *Hydrodynamics*, Cambridge Univ. Press, Cambridge, England, U.K., 1932.

[8]Batchelor, G. K., *An Introduction to Fluid Dynamics*, Cambridge Univ. Press, Cambridge, England, U.K., 1967.

[9]Shariff, K., Leonard, A., Zabusky, N. J., and Ferziger, J. H., "Acoustics and Dynamics of Coaxial Interacting Vortex Rings," *Fluid Dynamics Research*, Vol. 3, Nos. 1–4, 1988, pp. 337–343.

[10]Tang, S. K., and Ko, N. W. M., "On Sound Generated from the Interaction of Two Inviscid Coaxial Vortex Rings Moving in the Same Direction," *Journal of Sound and Vibration*, Vol. 187, No. 2, 1995, pp. 287–310.

[11]Verzicco, R., Iafrati, A., Riccardi, G., and Fatica, M., "Analysis of the Sound Generated by the Pairing of Two Axisymmetric Co-Rotating Vortex Rings," *Journal of Sound and Vibration*, Vol. 200, No. 3, 1997, pp. 347–358.

[12]Kambe, T., "Influence of Viscosity on Aerodynamic Sound Emission in Free Space," *Journal of Sound and Vibration*, Vol. 95, No. 3, 1984, pp. 351–360.

[13]Eldredge, J. D., Colonius, T., and Leonard, D., "A Dilating Vortex Particle Method for Compressible Flow," *Journal of Turbulence*, Vol. 3, No. 36, 2002, pp. 1–9.

[14]Lighthill, M. J., "On Sound Generated Aerodynamically. I General Theory," *Proceedings of the Royal Society*, Vol. A211, 1952, pp. 564–587.

[15]Crighton, D. G., "Computational Aeroacoustics for Low Mach Numbers," *Computational Aeroacoustics*, edited by J. C. Hardin and M. Y. Hussaini, Springer-Verlag, New York, 1992, pp. 50–68.

[16]Wells, V. L., and Renaut, R. A., "Computing Aerodynamically Generated Noise," *Annual Review of Fluid Mechanics*, Vol. 29, 1997, pp. 161–199.

[17]Tam, C. K. W., "Computational Aeroacoustics: Issues and Methods," *AIAA Journal*, Vol. 33, No. 10, 1995, pp. 1788–1796.

[18]Saffman, P. G., "The Velocity of Viscous Vortex Rings," *Studies in Applied Mathematics*, Vol. 49, No. 4, 1970, pp. 371–380.

[19]Bayliss, A., and Turkel, E., "Radiation Boundary Conditions for Wave-like Equations," *Communications in Pure and Applied Mathematics*, Vol. 33, Nov. 1980, pp. 707–725.

[20]Lee, D. J., and Koo, S. J., "Numerical Study of Sound Generation due to a Spinning Vortex Pair," *AIAA Journal*, Vol. 33, No. 1, 1995, pp. 20–26.

[21]Melander, M. V., Zabusky, N. I., and McWilliams, J. C., "Symmetric Vortex Merger in Two Dimensions: Causes and Conditions," *Journal of Fluid Mechanics*, Vol. 195, 1988, pp. 303–340.

[22]Inoue, O., and Hatakeyama, N., "Sound Generation by a Two-Dimensional Circular Cylinder in a Uniform Flow," *Journal of Fluid Mechanics*, Vol. 471, 2002, pp. 285–314.

[23]Dyson, F. W., "The Potential of an Anchor Ring, Part II," *Philosophical Transactions of the Royal Society of London*, Vol. A104, 1893, pp. 1041–1106.

A. Karagozian
Associate Editor